Research Article | Vol. 8, No. 11 | 1 Nov 2017 | BIOMEDICAL OPTICS EXPRESS 5228
Biomedical Optics EXPRESS

# Multimodal nonlinear optical imaging of unstained retinas in the epi-direction with a sub-40 fs Yb-fiber laser

GABRIELLE A. MURASHOVA,[1] CHRISTOPHER A. MANCUSO,[1] JACOB L. CANFIELD,[1] SANAE SAKAMI,[2] KRZYSZTOF PALCZEWSKI,[2] GRAZYNA PALCZEWSKA,[3] AND MARCOS DANTUS[1]

[1]*Department of Chemistry, Michigan State University, East Lansing, MI 48824, USA*
[2]*Department of Pharmacology, Case Western Reserve University, Cleveland, OH 44106, USA*
[3]*Department of Medical Devices, Polgenix Inc., Cleveland, OH 44106, USA*

**Abstract:** Ultrafast lasers have potential use in ophthalmology for diagnoses through non-invasive imaging as well as for surgical therapies or for evaluating pharmacological therapies. New ultrafast laser sources, operating at 1.07 µm and sub-40 fs pulse durations, offer exciting possibilities in multiphoton imagining of the retina as the bulk of the eye is relatively transparent to this wavelength, three-photon excitation is not absorbed by DNA, and this wavelength has a greater penetration depth compared to the commonly used 800 nm Ti:Sapphire laser. In this work, we present the first epi-direction detected cross-section and depth-resolved images of unstained isolated retinas obtained using multiphoton microscopy with an ultrafast fiber laser centered at 1.07 µm and a ~38 fs pulse duration. Spectral and temporal characterization of the autofluorescence signals show two distinct regions; the first one from the nerve fiber layer to the inner receptor layer, and the second being the retinal pigmented epithelium and choroid.



**OCIS codes**: (180.4315) Nonlinear microscopy; (170.3880) Medical and biological imaging; (140.3510) Lasers, fiber; (320.7090) Ultrafast lasers

## References and links

1. W. Denk, J. H. Strickler, and W. W. Webb, "Two-photon laser scanning fluorescence microscopy," Science **248**(4951), 73–76 (1990).
2. M. Müller, J. Squier, K. R. Wilson, and G. J. Brakenhoff, "3D microscopy of transparent objects using third-harmonic generation," J. Microsc. **191**(3), 266–274 (1998).
3. R. M. Williams, W. R. Zipfel, and W. W. Webb, "Interpreting second-harmonic generation images of collagen I fibrils," Biophys. J. **88**(2), 1377–1386 (2005).
4. P. Xi, Y. Andegeko, L. R. Weisel, V. V. Lozovoy, and M. Dantus, "Greater signal, increased depth, and less photobleaching in two-photon microscopy with 10 fs pulses," Opt. Commun. **281**, 1841–1849 (2008).
5. E. A. Gibson, O. Masihzadeh, T. C. Lei, D. A. Ammar, and M. Y. Kahook, "Multiphoton Microscopy for Ophthalmic Imaging," J. Ophthalmol. **2011**, 870879 (2011).
6. B. Nie, D. Pestov, F. W. Wise, and M. Dantus, "Generation of 42-fs and 10-nJ pulses from a fiber laser with self-similar evolution in the gain segment," Opt. Express **19**(13), 12074–12080 (2011).
7. D. Huang, E. A. Swanson, C. P. Lin, J. S. Schuman, W. G. Stinson, W. Chang, M. R. Hee, T. Flotte, K. Gregory, C. A. Puliafito, and J. G. Fujimoto, "Optical coherence tomography," Science **254**(5035), 1178–1181 (1991).
8. M. R. Hee, J. A. Izatt, E. A. Swanson, D. Huang, J. S. Schuman, C. P. Lin, C. A. Puliafito, and J. G. Fujimoto, "Optical coherence tomography of the human retina," Arch. Ophthalmol. **113**(3), 325–332 (1995).
9. M. Dantus, *Femtosecond Laser Shaping: From Laboratory to Industry* (CRC Press, 2017).
10. J. C. Sutherland and K. P. Griffin, "Absorption Spectrum of DNA for Wavelengths Greater than 300 nm," Radiat. Res. **86**(3), 399–409 (1981).
11. Y. Mattley, "Measuring DNA Absorbance with the STS-UV Microspectrometer," 1–3 (n.d.).
12. S. L. Jacques, "Physics in Medicine & Biology Optical properties of biological tissues: a review Optical properties of human tissues A N Bashkatov, E A Genina, V I Kochubey et al. - Optical absorption and scattering properties of bulk porcine muscle phantoms from int," Phys. Med. Biol. **58**, 2431 (2013).
13. F. Bevilacqua, D. Piguet, P. Marquet, J. D. Gross, B. J. Tromberg, and C. Depeursinge, "In vivo local determination of tissue optical properties: applications to human brain," Appl. Opt. **38**(22), 4939–4950 (1999).
14. S. Huang, A. A. Heikal, and W. W. Webb, "Two-photon fluorescence spectroscopy and microscopy of NAD(P)H and flavoprotein," Biophys. J. **82**(5), 2811–2825 (2002).

#303699 https://doi.org/10.1364/BOE.8.005228
Journal © 2017 Received 31 Jul 2017; revised 4 Oct 2017; accepted 4 Oct 2017; published 26 Oct 2017

Biomedical Optics EXPRESS


15. M. C. Skala, K. M. Riching, A. Gendron-Fitzpatrick, J. Eickhoff, K. W. Eliceiri, J. G. White, and N. Ramanujam, "In vivo multiphoton microscopy of NADH and FAD redox states, fluorescence lifetimes, and cellular morphology in precancerous epithelia," Proc. Natl. Acad. Sci. U.S.A. **104**(49), 19494–19499 (2007).
16. E. A. Gibson, O. Masihzadeh, T. C. Lei, D. A. Ammar, and M. Y. Kahook, "Multiphoton microscopy for ophthalmic imaging," J. Ophthalmol. **2011**, 870879 (2011).
17. S. He, C. Ye, Q. Sun, C. K. S. Leung, and J. Y. Qu, "Label-free nonlinear optical imaging of mouse retina," Biomed. Opt. Express **6**(3), 1055–1066 (2015).
18. J. M. Bueno, E. J. Gualda, and P. Artal, "Adaptive optics multiphoton microscopy to study ex vivo ocular tissues," J. Biomed. Opt. **15**(6), 066004 (2010).
19. F. Aptel, N. Olivier, A. Deniset-Besseau, J.-M. Legeais, K. Plamann, M.-C. Schanne-Klein, and E. Beaurepaire, "Multimodal Nonlinear Imaging of the Human Cornea," Invest. Ophthalmol. Vis. Sci. **51**(5), 2459–2465 (2010).
20. D. Débarre, W. Supatto, A.-M. Pena, A. Fabre, T. Tordjmann, L. Combettes, M.-C. Schanne-Klein, and E. Beaurepaire, "Imaging lipid bodies in cells and tissues using third-harmonic generation microscopy," Nat. Methods **3**(1), 47–53 (2006).
21. O. Masihzadeh, T. C. Lei, S. R. Domingue, M. Y. Kahook, R. A. Bartels, and D. A. Ammar, "Third harmonic generation microscopy of a mouse retina," Mol. Vis. **21**, 538–547 (2015).
22. G. Palczewska, A. Maeda, M. Golczak, E. Arai, Z. Dong, L. Perusek, B. Kevany, and K. Palczewski, "Receptor MER tyrosine kinase proto-oncogene (MERTK) is not required for transfer of bis-retinoids to the retinal pigmented epithelium," J. Biol. Chem. **291**(52), 26937–26949 (2016).
23. R. W. Young and D. Bok, "Participation of the retinal pigment epithelium in the rod outer segment renewal process," J. Cell Biol. **42**(2), 392–403 (1969).
24. M. L. Katz, W. L. Stone, and E. A. Dratz, "Fluorescent pigment accumulation in retinal pigment epithelium of antioxidant-deficient rats," Invest. Ophthalmol. Vis. Sci. **17**(11), 1049–1058 (1978).
25. J. J. Weiter, F. C. Delori, G. L. Wing, and K. A. Fitch, "Retinal pigment epithelial lipofuscin and melanin and choroidal melanin in human eyes," Invest. Ophthalmol. Vis. Sci. **27**(2), 145–152 (1986).
26. F. C. Delori, C. K. Dorey, G. Staurenghi, O. Arend, D. G. Goger, and J. J. Writer, "In Vivo Fluorescence of the Ocular Fundus Exhibits Retinal Pigment Epithelium Lipofuscin Characteristics," Investigative Ophthalmol. Vis. Sci. **36**, 718–729 (1995).
27. C. J. Kennedy, P. E. Rakoczy, and I. J. Constable, "Lipofuscin of the retinal pigment epithelium: a review," Eye (Lond.) **9**(Pt 6), 763–771 (1995).
28. F. Holz, R. Spaide, A. C. Bird, and S. Schmitz-Valckenberg, "Lipofuscin of the Retinal Pigment Epithelium," in *Atlas of Fundus Autofluorscence Imaging* (Springer Berlin Heidelberg, 2007), pp. 3–16.
29. D. Schweitzer, S. Schenke, M. Hammer, F. Schweitzer, S. Jentsch, E. Birckner, W. Becker, and A. Bergmann, "Towards metabolic mapping of the human retina," Microsc. Res. Tech. **70**(5), 410–419 (2007).
30. S. Warburton, W. E. Davis, K. Southwick, H. Xin, A. T. Woolley, G. F. Burton, and C. D. Thulin, "Proteomic and phototoxic characterization of melanolipofuscin: correlation to disease and model for its origin," Mol. Vis. **13**, 318–329 (2007).
31. C. A. Curcio and M. Johnson, "Structure, Function, and Pathology of Bruch's Membrane," in *Retina Fifth Edition* (2012), Vol. 1, pp. 465–481.
32. J. R. Sparrow, E. Gregory-Roberts, K. Yamamoto, A. Blonska, S. K. Ghosh, K. Ueda, and J. Zhou, "The bisretinoids of retinal pigment epithelium," Prog. Retin. Eye Res. **31**(2), 121–135 (2012).
33. M. E. Boulton, "Studying melanin and lipofuscin in RPE cell culture models," Exp. Eye Res. **126**, 61–67 (2014).
34. J. R. Sparrow and T. Duncker, "Fundus Autofluorescence and RPE Lipofuscin in Age-Related Macular Degeneration," J. Clin. Med. **3**(4), 1302–1321 (2014).
35. Y. Coello, B. Xu, T. L. Miller, V. V Lozovoy, and M. Dantus, "Group-velocity dispersion measurements of water, seawater, and ocular components using multiphoton intrapulse interference phase scan," (n.d.).
36. Y. Coello, V. V. Lozovoy, T. C. Gunaratne, B. Xu, I. Borukhovich, C. Tseng, T. Weinacht, and M. Dantus, "Interference without an interferometer: a different approach to measuring, compressing, and shaping ultrashort laser pulses," J. Opt. Soc. Am. B **25**, A140 (2008).
37. H. Gross, F. Blechinger, and B. Achtner, "Handbook of optical systems, Volume 4: Survey of optical instruments," Handb. Opt. Syst. **4**, 1092 (2008).
38. L. I. of America and N/A, *ANSI Z136.1 - Safe Use of Lasers* (2014).
39. V. V. Lozovoy, I. Pastirk, and M. Dantus, "Multiphoton intrapulse interference. IV. Ultrashort laser pulse spectral phase characterization and compensation," Opt. Lett. **29**(7), 775–777 (2004).
40. P. Xi, Y. Andegeko, D. Pestov, V. V. Lovozoy, and M. Dantus, "Two-photon imaging using adaptive phase compensated ultrashort laser pulses," J. Biomed. Opt. **14**(1), 014002 (2009).
41. T. E. Oliphant, "Python for scientific computing," Comput. Sci. Eng. **9**, 10–20 (2007).
42. N. L. Mata, J. Weng, and G. H. Travis, "Biosynthesis of a major lipofuscin fluorophore in mice and humans with ABCR-mediated retinal and macular degeneration," Proc. Natl. Acad. Sci. U.S.A. **97**(13), 7154–7159 (2000).
43. L. K. Barthel and P. A. Raymond, "Improved method for obtaining 3-microns cryosections for immunocytochemistry," J. Histochem. Cytochem. **38**(9), 1383–1388 (1990).
44. M. W. Conklin, P. P. Provenzano, K. W. Eliceiri, R. Sullivan, and P. J. Keely, "Fluorescence lifetime imaging of endogenous fluorophores in histopathology sections reveals differences between normal and tumor epithelium in carcinoma in situ of the breast," Cell Biochem. Biophys. **53**(3), 145–157 (2009).
45. P. V. Sarthy and D. M. Lam, "Isolated cells from a mammalian retina," Brain Res. **176**(1), 208–212 (1979).

Biomedical Optics EXPRESS

46. J. R. Sparrow, C. A. Parish, M. Hashimoto, and K. Nakanishi, "Pigmented Epithelial Cells in Culture," Invest. Ophthalmol. Vis. Sci. **40**, 2988–2995 (1999).
47. M. Balu, I. Saytashev, J. Hou, M. Dantus, and B. J. Tromberg, "Sub-40 fs, 1060-nm Yb-fiber laser enhances penetration depth in nonlinear optical microscopy of human skin," J. Biomed. Opt. **20**(12), 120501 (2015).
48. M. Boulton, F. Docchio, P. Dayhaw-Barker, R. Ramponi, and R. Cubeddu, "Age-related changes in the morphology, absorption and fluorescence of melanosomes and lipofuscin granules of the retinal pigment epithelium," Vision Res. **30**(9), 1291–1303 (1990).
49. S. Watanabe, G. Matthews, M. L. Woodruff, I. V. Peshenko, A. B. Savchenko, C. L. Makino, Y.-S. Ho, G. L. Fain, and A. M. Dizhoor, "Regional distribution of cGMP-activated ion channels in the plasma membrane of the rod photoreceptor," J. Neurosci. **8**(7), 2334–2337 (1988).
50. B. Chang, N. L. Hawes, R. E. Hurd, M. T. Davisson, S. Nusinowitz, and J. R. Heckenlively, "Retinal degeneration mutants in the mouse," Vision Res. **42**(4), 517–525 (2002).
51. M. Hoon, H. Okawa, L. Della Santina, and R. O. L. Wong, "Functional architecture of the retina: development and disease," Prog. Retin. Eye Res. **42**, 44–84 (2014).
52. I. Rocha-Mendoza, D. R. Yankelevich, M. Wang, K. M. Reiser, C. W. Frank, and A. Knoesen, "Sum Frequency Vibrational Spectroscopy: The Molecular Origins of the Optical Second-Order Nonlinearity of Collagen," Biophys. J. **93**(12), 4433–4444 (2007).
53. R. W. Boyd, *Nonlinear Optics* (Academic Press, 2008).
54. F. Aptel, N. Olivier, A. Deniset-Besseau, J. M. Legeais, K. Plamann, M. C. Schanne-Klein, and E. Beaurepaire, "Multimodal nonlinear imaging of the human cornea," Invest. Ophthalmol. Vis. Sci. **51**(5), 2459–2465 (2010).
55. O. Masihzadeh, T. C. Lei, S. R. Domingue, M. Y. Kahook, R. A. Bartels, and D. A. Ammar, "Third harmonic generation microscopy of a mouse retina," Mol. Vis. **21**, 538–547 (2015).
56. A. D. Marmorstein, L. Y. Marmorstein, H. Sakaguchi, and J. G. Hollyfield, "Spectral Profiling of Autofluorescence Associated with Lipofuscin, Bruch ' s Membrane, and Sub-RPE Deposits in Normal and AMD Eyes," Invest. Ophthalmol. Vis. Sci. **43**, 2435–2441 (2017).
57. W. A. N., William A. N. Dorland, *Dorland's Illustrated Medical Dictionary*. (Saunders/Elsevier, 2012).
58. M. L. Katz, C.-L. Gao, and L. M. Rice, "Formation of lipofuscin-like fluorophores by reaction of retinal with photoreceptor outer segments and liposomes," Mech. Ageing Dev. **92**(2-3), 159–174 (1996).
59. W. G. Robison and M. L. Katz, *Vitamin A and Lipofuscin* (Springer New York, 1987), pp. 95–122.
60. J. R. Sparrow, Y. Wu, T. Nagasaki, K. D. Yoon, K. Yamamoto, and J. Zhou, "Fundus autofluorescence and the bisretinoids of retina," Photochem. Photobiol. Sci. **9**(11), 1480–1489 (2010).

## 1. Introduction

With the goal of exploring the feasibility of novel retinal diagnostics and therapies, we evaluate the use of unstained multimodal nonlinear optical imaging techniques [1–5] with a compact femtosecond fiber laser [6]. While advances in optical coherence tomography (OCT) have made retinal imaging widely accessible in the clinic [7,8], there is room for improvement with respect to providing chemical as well as subcellular resolution. Moreover, the sub-40 fs Yb-fiber laser centered at 1.07 μm being considered here for multimodal imaging could in principle be used for diagnostic imaging as well as for performing therapeutic treatments [9]. Here, we explore the use of this laser for retinal imaging. When compared to a 800 nm Ti:Sapphire laser, the longer central wavelength is advantageous because the absorption of DNA at 355 nm (3-photon of 1.07 μm) is at least 5 orders of magnitude weaker than at 266 nm (3-photon of 800 nm) [10,11]. Furthermore, scattering decreases for longer wavelengths, which for retinal tissues can be estimated to be 28% less for the longer wavelength [12,13], allowing greater imaging depth.

In multiphoton biomedical imaging contrast arises from several different nonlinear optical processes, such as two-photon excited fluorescence (2PEF), three-photon excited fluorescence (3PEF), second harmonic generation (SHG), and third harmonic generation (THG), which are greatly enhanced at the focal plane [1–5]. Multiphoton autofluorescence from nicotinamide adenine dinucleotide (NADH) and flavin adenine dinucleotide (FAD) are conventionally used in biomedical imaging for diagnosis and monitoring the metabolic activity of cells [14,15]. Label-free nonlinear optical imaging of retina has been reported using a Ti:Sapphire [16–20] and also with a Yb-fiber laser detecting THG in the forward direction and 2PEF in the epi direction [21]. Specifically from the retina, multiphoton emission has been found from lipofuscin and di-retinoid-pyridinium-ethanolamine (A2E) [22]. This is significant because lipofuscin and A2E emissions have been used to diagnose retinal diseases such as age-related macular degeneration [23–34].

Biomedical Optics EXPRESS

While this work presents the feasibility for an *in vivo* imaging system for retinal disease diagnosis, many additional studies will be needed to address technical limitations. Among the different limitations to be addressed, is the need for adaptive compression of the femtosecond laser pulses to account for the dispersion introduced by the cornea, lens, and vitreous humor. Fortunately, the dispersion introduced by those tissues has been measured and adaptively compensated [35,36]. Similarly, there may be the need for adaptive optics to adjust the focus of the laser in order to compensate for diffractive imperfections amongst different eyes, as well as for the limited numerical aperture (NA) of the eye [18,37]. In terms of safety, the ANSI standards limit eye exposure from a laser at ~1.07 μm to 4 mW, assuming a dilated pupil [38]. This value does not take into account the use of adaptive optics which would be used to improve focusing at the retina. Once these technical issues are addressed, validating the diagnosis of healthy retina animal models as well as diseased retina animal models, using this system, will need to be done. Finally, human trials would be required once all of the preliminary studies are completed successfully.

In this work, we present the first all epi-direction images of unstained mouse retinas and a Cynomolgus monkey retina using a 1.07 μm Yb-fiber ultrafast laser with a ~38 fs pulse duration. Epi- as opposed to forward-direction detection was chosen as it is the only collection geometry that would permit *in vivo* imaging. In addition, we measure both the spectra and lifetimes across the retinal layers from 7 μm-thick cross-sections of mouse retinas. The spectroscopic and lifetime information that becomes accessible through multimodal imaging, as performed here, may in the future provide the functional imaging at sub-cellular resolution that is presently missing from retinal diagnosis. Furthermore, the laser being used may at some point be evaluated for its ability to perform therapeutic interventions such as cauterization with greatly enhanced three-dimensional accuracy, as compared to present continuous wave lasers.

## 2. Materials and methods

### *Signal source, acquisition, and processing*

The custom designed laser source for our multiphoton microscope is a Yb-fiber laser oscillator producing pulses with sub-40 fs pulse durations (full-width half-maximum) (1.07 μm, 42 MHz) [6] (Fig. 1). The microscope used was a Nikon TE2000 in the inverted configuration. For imaging, a 40x water immersion objective was employed with a working distance of 0.5 mm (Zeiss LD-C APOCHROMAT 1.1NA, Jena, Germany) to focus the beam on the retina to a beam waist (diameter of the beam at the focus) of ~0.5 μm, allowing the generation of peak intensities high enough to induce multiphoton processes with less than 7 mW of average power and pulse durations of 38 ± 1 fs. Thus, minimizing the effects of photobleaching and thermal damage. Laser scanning was done with galvanometer mirrors. The peak intensity was maximized through the use of a pulse-shaper (MIIPS HD, BioPhotonic Solutions Inc., East Lansing, MI, USA) to compensate for the high-order dispersion along the beam path [36,39,40].

Signal detection was accomplished in the epi-direction with two separate detection systems. To obtain frequency and time-resolved data a time-correlated single photon-counting (TCSPC) system with a compact spectrometer and a 16-photomultiplier tube (PMT) array were used (SPC-830 TCSPC, Becker-Hickl, GmBH). The spectral resolution of the TCSPC system is ~12.5 nm, limited by the physical size of each PMT in the array and confirmed with a mercury lamp. The grating in the spectrometer was rotated to select different spectral regions. Here two grating positions were used to collect the fluorescence spectra; one with a collection range from ~300 nm to ~500 nm and the other from ~480 nm to ~680 nm. The images of the sliced mouse retinas obtained using the TCSPC were imaged with 6.9 mW of power or less for a total exposure time of 4.5 minutes (90 seconds per grating position).

The lifetime curves had a collection window of 12.5 ns, chosen because it is four times longer than the longest observed emission lifetime and not limited by the repetition rate of the

Biomedical Optics EXPRESS

laser. The analogue to digital converter (ADC) resolution was set to 256 time bins. The first two nanoseconds before the rise of the lifetime signal peak were used for background subtraction. The instrument response function (IRF) was measured to be ~110 ps. Fits for the lifetimes were done in Python using the curve-fit function in module scipy.optimize [41]. No efforts were made to deconvolve the IRF in the fits. However, this should only slightly affect fit values for lifetimes that are close to the IRF.

Depth resolved imaging of the unstained Cynomolgus monkey flat mount was done with the same system as the sliced mouse retinas, however the emission was collected with a single PMT (HC2005MOD, Hamamatsu) instead of the TCSPC. To achieve depth imaging, the focal plane depth was scanned by a motorized stage (Focus Drive with Integrated Controller by TOFRA, Inc. Palo Alto, California) which was controlled by a home-built data acquisition program in LABVIEW (Dr. Peng Xi, Dantus Research Group, Michigan State University). The depth resolved images were acquired for a total depth of 220 μm, with a 0.05-μm step in between each 2D-512x512 pixel image. Depth resolution is estimated to be ~1 μm, however, oversampling in depth allowed us room to average a few images at each depth. Each 2D image was averaged for 5 seconds. Depth resolved imaging was done using a constant laser power of 7 mW through all the retinal layers.

### *Preparation of fixed and unfixed thin sliced mouse retinas*

The C57BL/6 mice were purchased from the Jackson Laboratory (Bar Harbor, ME, USA) and were raised in a 12-hour light/12-hour dark cyclic environment and maintained on a standard diet at the Case Western Reserve University, School of Medicine animal resources facility. It is known that when B6 mice are raised under cyclic light conditions (12 hours of light and 12 hours of darkness), A2E— the major component of lipofuscin, increases only moderately up to the age of 18 weeks [42]. The fixed thin retinal sections were prepared as follows: eyeballs were obtained from post-natal day (PND) 14 male pup of C57BL/6 mice immediately after euthanasia. Eyeballs were fixed with 4% paraformaldehyde in phosphate buffered saline (PBS, 136 mM NaCl, 2 mM KCl, 8 mM Na2HPO4, and 1 mM KH2PO4, pH 7.4) containing 5% sucrose for short time. Then, their cornea and lens were removed in PBS solution. Resulting eyecups were fixed for 2.5 hours at 4 °C with gentle agitation. After fixation, eyecups were dehydrated with increasing series of sucrose in PBS and then infiltrated with a 2:1 mixture of 20% sucrose /PBS and optimal cutting temperature (OCT) compound (Sakura) [43]. Eyecups were then frozen using 2-Methylbutane cooled with liquid $N_2$. The unfixed thin sliced retina was prepared from a PND 80 ± 3 female mouse. The procedure of sample preparation is similar to that described for fixed retina preparation with the following modifications: 1) their cornea and lens were removed in Hank's Balanced Salt Solution (Thermo Fisher Scientific, Waltham, MA, cat. no. 14175095), 2) immediately after the dissection, resulting eyecups were transferred into a 2:1 mixture of 20% sucrose/PBS and OCT compound, and 3) eyecups were incubated for 5 minutes and then frozen. Cryo-sections (7 μm) of the retinas were prepared with cryostat –microtome (CM1850, Leica, Bannockburn, IL). While cryo-preservation methods have been known to cause deleterious effects on endogenous fluorescence, it was reported [44] that endogenous fluorescence of FAD and NAD(P)H were preserved during fixation, paraffin-embedding, and subsequent slide preparation. In this work, we used less destructive cryo-preservation methods. Thus, unlike the paraffin-embedding method, tissue was not dehydrated with 100% ethanol and Xylene. Therefore, greater expected preservation of endogenous fluorescence is expected when compared to paraffin-embedding method— which is already known not to affect coenzyme fluorescence. Sections were dried at room temperature for ~2 hours for unfixed conditions and overnight at 37°C for fixed conditions. Then, sections were rehydrated with PBS for 20 minutes. Rehydrated sections were mounted in an imaging medium {glycerol 85% w/vol (Fisher Scientific, Pittsburgh, PA, cat. no. G-31), Mowiol4-88 15% w/vol (Millipore Sigma, Billerica, MA, cat. no. 475904) in Mammalian Ringer's solution [45]} and covered with #1.5

Biomedical Optics EXPRESS

coverslips. Slides were kept at 4 °C. Unfixed retinal sections were imaged within 2 days. It is important to note that fixation with paraformaldehyde has been known to shift the emission peaks of molecules found in the retina [46], however, these shifts are usually small (~5 nm) and do not impact the findings of this manuscript. All procedures and experiments were approved by the Institutional Animal Care and Use Committee (IACUC, Case Western Reserve University) and conformed to the recommendations of both the American Veterinary Medical Association Panel on Euthanasia and the Association of Research for Vision and Ophthalmology

### *Preparation of fixed flat mount monkey retina*

The Cynomolgus monkey was raised in a 12-hour light/12-hour dark cyclic environment and maintained on a standard diet at Ricerca Biosciences LLC, Painesville, OH. Ricerca Biosciences collected a fresh eyeball from a 4-year-old male Cynomolgus monkey after euthanasia. The eyeball was washed with PBS three times. Then, the cornea, lens, and vitreous were removed in PBS solution. Next, retina was separated from RPE and four slits were made to the retina. The retina was then flattened in a cell culture dish with ganglion cell-side up. Following so, the flattened retina was fixed with 4% paraformaldehyde in PBS for 6 hours at 4 °C. After the fixation, the retina was washed with PBS and transferred onto a large glass slide with the ganglion cell side up (EMS, Hatfield, PA, cat. no. 71862-01). The flattened retina was mounted in the imaging medium and covered with a #1 coverslip (EMS, cat.no. 63774-01). The retina was kept at 4 °C until it was imaged.

### *Preparation of reference solutions*

Reference solutions of FAD and NADH were prepared by performing a 1:10 dilution of 10X PBS (Dot Scientific Inc.). The dilution was performed using MilliQ water. Thirty milligrams (mg) of each compound was added to separate solutions in PBS (136 mM NaCl, 2 mM KCl, 8 mM $Na_2HPO_4$, 1mMKH2PO4, pH7.4) yielding concentrations of approximately 350 µM for NADH (Sigma Aldrich) and 300 µM for FAD (Sigma Aldrich). An A2E reference solution was prepared using a 10 mM stock solution diluted in dimethyl sulfoxide to yield a final 1 mM concentration. A drop of each solution was placed on a microscope slide (Corning) followed by a coverslip (Corning) and then placed coverslip-side down on the microscope objective. Water based immersion fluid (Zeiss, ImmersolTM, $n_e$ = 1.334 (23°C), $v_e$ = 85) was used to increase the numerical aperture (NA) between the coverslip and the microscope objective.

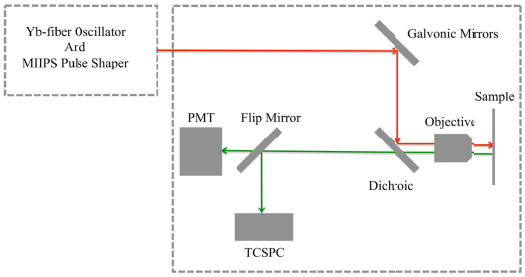


Fig. 1. The experimental apparatus consisted of an ultrafast fiber laser operating at 1.07 µm, a MIIPS pulse shaper, a laser scanning inverted microscope, and a photon detector, mounted in the epi-direction. The TCSPC was used to collect fluorescence spectra and lifetime, whereas the single PMT was used to acquire the depth resolved images.

## 3. Results

The multimodal images in Fig. 2 present all the retinal layers, including the nerve fiber layer (NFL), ganglion cell layer (GCL), inner plexiform layer (IPL), inner nuclear layer (INL), outer plexiform layer (OPL), outer nuclear layer (ONL), inner receptor layer (IRL), outer

Biomedical Optics EXPRESS

receptor layer (ORL), and retinal pigment epithelium (RPE), as well as the choroid and sclera. In Fig. 2(a), the blue, green, and red channels represent emission centered at 535 nm, 575 nm, and 629 nm, respectively. Subsequently, the blue, green, and red channels in Fig. 2(b) represent emission centered at 355 nm, 535 nm, and 629 nm. Each channel in both Fig. 2(a) and 2(b) have a spectral bandwidth of ~37.5 nm. Here, 355 nm and 535 nm correspond to THG and SHG, respectively. Further information for how the other wavelengths were chosen can be found in the Discussions section.

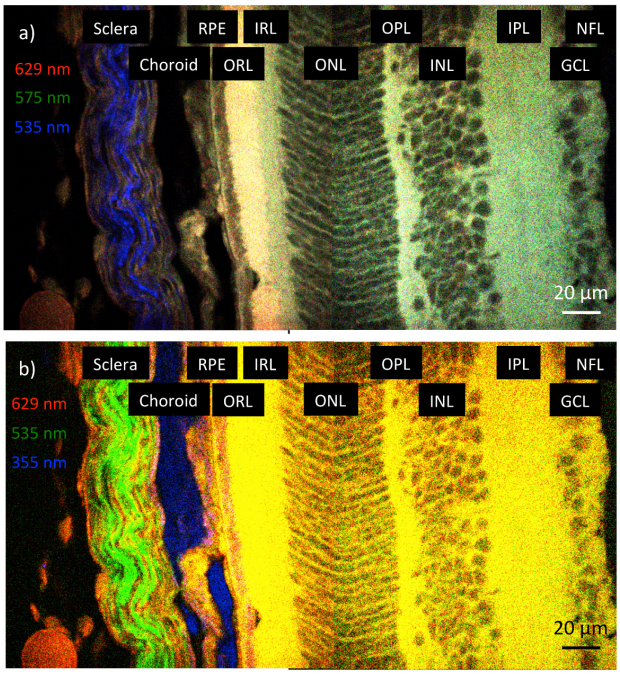


Fig. 2. Three colored (red, green, blue) composite multimodal images of the retinal layers from a 7 µm slice of a mouse retina taken with the TCSPC at 6.9 mW of power depths using a 1.07 µm Yb-fiber laser with 35.0 fs pulse durations. Image acquisition was done at 30-second intervals for a total of 4.5 minutes. (a) Here the blue, green, and red channels represent emission centered at 535 nm, 575 nm, and 629 nm, respectively. (b) The blue, green, and red channels represent emission centered at 355 nm, 535 nm, and 629 nm, respectively. The bandwidth of each channel is ~37.5 nm.

In Fig. 3(a)-3(b) we plotted the lineouts of the spectral components from the multimodal images (Fig. 2). In each of these figures the data are comprised of the sum of all pixels in a slice of each layer. The same sized slice was taken for each layer (~5 µm x 85 µm) to most accurately compare the emission spectra and emission yield across the layers. Although this prevents measuring the inhomogeneity in each retinal layer, the data were analyzed as such to achieve an acceptable signal-to-noise ratio. The emission spectra (Fig. 3(a)) show that the strongest fluorescence is seen in the receptor layers (ORL and IRL). When the emission spectra are normalized to the maximum value for each layer (Fig. 3(b)), it can be seen that the spectral shape of the emission is nearly identical in the most anterior layers of the retina (NFL through the OPL), with a maximum near 560 nm. The more proximal retinal layers, from the ONL to the choroid bear a greater signal at wavelengths > 600 nm. At the most posterior portion of the ocular tissue, the sclera has the most unique spectrum, displaying a peak at ~535 nm, that we attribute to SHG (see Discussion). Here, only a plot for the spectral range of 480-680 nm is shown, as the only emission below 480 nm that could be characterized was a small amount of THG from the choroid, RPE, and sclera. No attempts were made at spectral unmixing as not all fluorophores contributing to emission spectrum were identified, and we

Biomedical Optics EXPRESS

were unable to obtain pure lipofuscin, which we believe to be a major component of the emission spectrum.

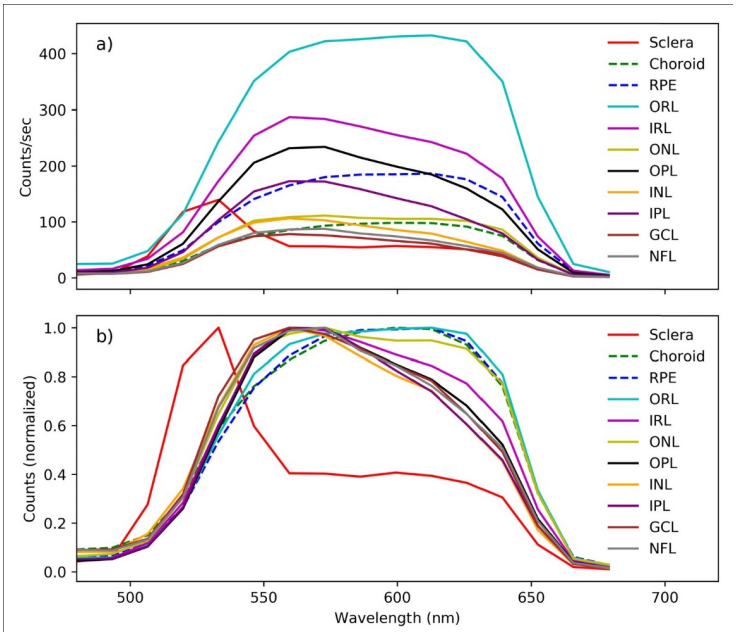


Fig. 3. Spectral emission from 480 to 680 nm detected from a mouse retina. a) The non-normalized emission spectra reveal that the receptor layers (ORL and IRL) have the strongest fluorescence emission. b) The normalized spectra more readily compare the different spectral shapes across retinal layers. Layers from the NFL thru the OPL all have nearly identical spectral shapes. The sclera has a unique spectral shape, where the peak at 535 nm is attributed to SHG (see Discussion).

The lifetimes across the retinal layers are presented for two spectral regions, 556-594 nm (Fig. 4(a), 4(c)) and 610-648 nm (Fig. 4(b), 4(c)). Both spectral regions show two characteristic lifetimes across the retinal layers. These two lifetimes can be grouped as a "longer" lifetime seen in the layers from the NFL through the ORL and the sclera, and a "shorter" lifetime seen in the RPE and choroid. Interestingly, the lifetimes for the RPE and choroid become shorter at longer detection wavelengths (i.e. from Fig. 4(a) to Fig. 4(b)). This trend is shown directly in panel c, where the lifetimes for the choroid through the IPL are fitted for both the short wavelength range and the long wavelength range. In addition, we have also plotted in Fig. 4(c) the lifetime measured from the sclera at 535 nm. The emission is dominated by SHG from collagen, and coincides with the measured IRF of our system (~110 ps).

Biomedical Optics EXPRESS

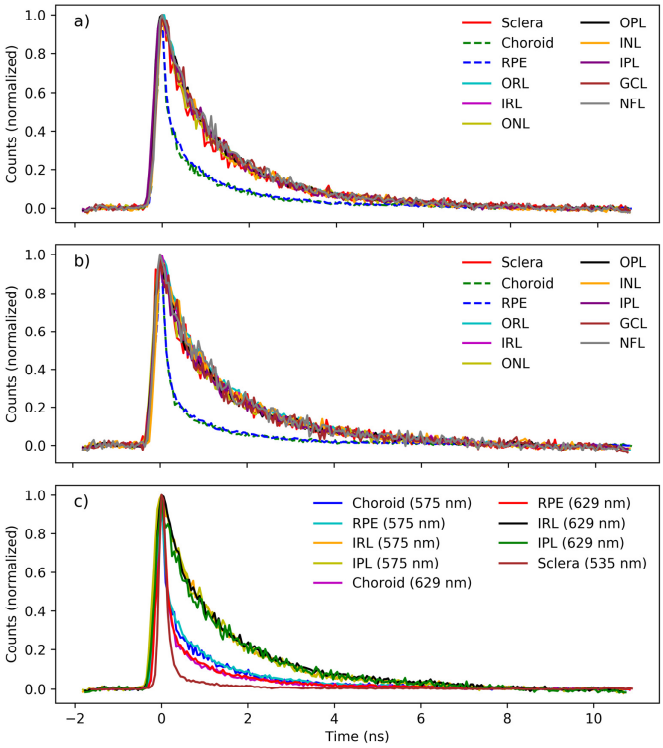


Fig. 4. Fluorescence lifetimes across the retinal layers from a mouse over a spectral range of a) 556-594 nm, b) 610-648 nm, and c) short: 556-594 nm and long: 610-648 nm. The plots reveal that for a given spectral band, all the layers from the NFL through the ORL have nearly identical lifetimes, whereas the choroid and RPE have nearly identical lifetimes. Additionally, the lifetimes in the choroid and RPE become shorter for longer detection wavelengths (i.e. from panel a to panel b). This trend is shown directly in panel c, where the lifetimes for the choroid, RPE, IRL, and IPL are fitted for both the short wavelength range and the long wavelength range. Also in panel c is the lifetime measured at 535 nm from the sclera. SHG from collagen in the sclera is the source of this emission and coincides with the IRF of our system.

The copious lifetime curves, and their accompanying parameters necessary to measure the fits for Fig. 4, could not be effectively presented alongside each curve in the figure. Therefore, the fitting parameters and their calculated values for the lifetime decays shown in Figs. 4(a)-4(b) are presented in Table 1 and Table 2. Given the similarities in the measured lifetimes from the ORL through the NFL layers (within 5%), we summed them together. The same was done for signals from the choroid and RPE, prior to fitting. Two different sets of fitting methods were used: mono- and bi-exponential fits for the ORL through the NFL and bi- and tri-exponential fits for the choroid and RPE. The fits were performed over two wavelength ranges: 556-594 nm and 610-648 nm. Tri-exponential fit values were excluded from Table 1 and Table 2 for the ORL-NFL considering that the $t_2$ and $t_3$ values were equal. Likewise, mono-exponential fit values were excluded from Table 1 and Table 2 for the RPE and choroid, as all of the fits had an $R^2$ value of less than 0.91. Additional information on the fits, representative lifetime decay data, including why certain fits were excluded, can be found in Appendix 1.

Biomedical Optics EXPRESS

**Table 1. Lifetime fitting of data shown in Fig. 4. The parenthetical values correspond to one standard deviation. $R^2$ is the coefficient of determination, a dimensionless quantity.**

| Lifetime Decays with Fixed Parameters | | | | | | | | | | | | | |
|---|---|---|---|---|---|---|---|---|---|---|---|---|---|
| | 556-594 nm | | | | | | 610-648 nm | | | | | |
| ORL through NFL | Mono Fit (ns) | | | | | | Mono Fit (ns) | | | | | |
| | $t_1$(ns) | $R^2$ | | | | | $t_1$(ns) | $R^2$ | | | | |
| | 1.326 (0.009) | 0.99 | | | | | 1.255 (0.014) | 0.98 | | | | |
| | Bi Fit (ns) | | | | | | Bi Fit (ns) | | | | | |
| | $a_1$ | $t_1$(ns) | $a_2$ | $t_2$(ns) | $R^2$ | | $a_1$ | $t_1$(ns) | $a_2$ | $t_2$(ns) | $R^2$ | |
| | 0.595 (0.008) | 0.880 (0.040) | 0.405 (0.049) | 2.158 (0.108) | 1 | | 0.376 (0.018) | 0.451 (0.023) | 0.624 (0.018) | 1.872 (0.035) | 1 | |
| Choroid and RPE | Bi Fit (ns) | | | | | | Bi Fit (ns) | | | | | |
| | $a_1$ | $t_1$(ns) | $a_2$ | $t_2$(ns) | $R^2$ | | $a_1$ | $t_1$(ns) | $a_2$ | $t_2$(ns) | $R^2$ | |
| | 0.640 (0.005) | 0.121 (0.003) | 0.360 (0.005) | 1.408 (0.022) | 0.99 | | 0.807 (0.007) | 0.174 (0.004) | 0.193 (0.007) | 1.765 (0.066) | 0.99 | |
| | Tri Fit (ns) | | | | | | Tri Fit (ns) | | | | | |
| | $a_1$ | $t_1$(ns) | $a_2$ | $t_2$(ns) | $a_3$ | $t_3$(ns) | $R^2$ | $a_1$ | $t_1$(ns) | $a_2$ | $t_2$(ns) | $a_3$ | $t_3$(ns) | $R^2$ |
| | 0.530 (0.010) | 0.091 (0.003) | 0.323 (0.011) | 0.669 (0.042) | 0.151 (0.015) | 2.334 (0.116) | 1 | 0.829 (0.017) | 0.153 (0.005) | 0.177 (0.047) | 01.168 (0.333) | 0.053 (0.059) | 3.111 (1.434) | 0.99 |

Having established the nonlinear optical signals from the different retinal layers from thin-sliced mouse retinas, we performed depth-resolved imaging on an unstained fixed Cynomolgus monkey retina flat mount with a thickness of 220 µm. We were fortunate this retina became available as it most closely resembles the histology of a human retina. Single PMT signal detection allowed the collection of multiple photons per laser pulse (unlike TCSPC, for which fewer than one photon per pulse is the standard). Single PMT signals, however, lack spectral and temporal information. Figure 5 shows an 8-panel image of 2D slices of the retina at different depths. To assess the potential for *in vivo* imaging of human retinas with 1.07 µm and sub-40 fs (34.8 fs) laser pulses, we used the flat mount configuration, as flat mounts are more representative of the geometry (the orientation of the plane of the retina to the incoming laser pulse) that is need *in vivo*.

In addition to being the first epi-direction detected multimodal images of a retina, the quality of the images is excellent. We attribute the quality of the images to the use of sub-50 fs pulses, a high NA objective, and the use of a longer wavelength 1.07 µm laser with longer scattering length [12,13,47]. In addition, we imaged in 0.05 µm *z*-steps so that averaging could be done for each retinal layer. The depth-resolved image in Fig. 5 shows sub-cellular resolution at each layer, with morphological characteristics of specific layers being easily distinguishable. For example, nerve fibers in the NFL, ganglion cells in the GCL, cell nuclei in the INL, receptor cell nuclei in the ONL, inner segments of cone photoreceptors (large white features) and rod photoreceptor inner segments (smaller round features between the cone inner segments) in the IRL. Additionally, the ability to visualize details of the IPL and OPL layers is fascinating considering these layers are quite thin. This level of resolution, which could include additional wavelength channels, could be of importance for the diagnosis of retinal and ocular disorders, especially when observing the structural organization of the rods and cones in instances of retinitis pigmentosa, cone-rod dystrophy, as well as other retinal diseases associated with the sclera and composition of the retinosomes present in the RPE [48–51].

Biomedical Optics EXPRESS

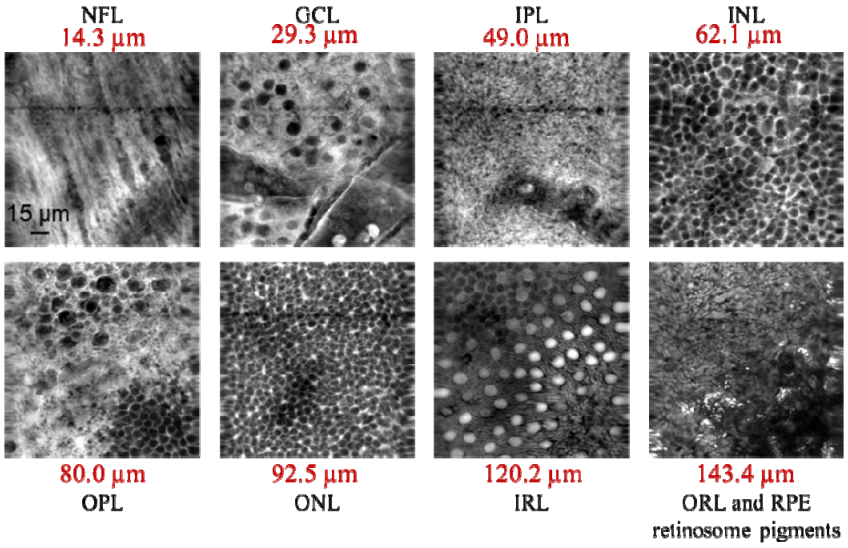


Fig. 5. Depth-resolved imaging of an unstained, fixed, Cynomolgus monkey retina flat mount. The total extent of the Cynomolgus monkey retina was 220 µm. The depth of each image is indicated in yellow. The scale bar is 15 µm and can be seen in the NFL panel. Each 2D image was an average of 5 scans, averaged for 5 seconds. Each layer, beginning with the NFL and ending with the ORL and RPE retinosomes, from left to right, was an average of 182 images (9.1 µm), 190 images (9.5 µm), 182 images (9.1 µm), 139 images (7.0 µm), 51 images (2.63 µm), 233 images (11.7 µm), 211 images (10.6 µm), and 33 images (1.7 µm), respectively. The depth resolved stack was obtained with 7 mW of average power at all depths using a 1.07 µm Yb-fiber laser with 34.8 fs pulse durations. In the IRL, inner segments of cone photoreceptors (large white features) and rod photoreceptor inner segments (smaller round features between the cone inner segments) are easily distinguishable. We believe that the bright particles in the bottom right panel are perhaps melanin or RPE retinosomes attached to the tips of photoreceptors. At each depth, the characteristic morphology of the retina layers is clear, indicating that the Yb-fiber laser is effective at achieving the cellular resolution needed for depth resolved imaging. Video of depth resolved imaging of retina used to obtain the images presented in this figure (Visualization 1).

## 4. Discussion

With the work presented here, we have begun the initial studies required to propose use of the 1.07 µm Yb-fiber laser for label free non-invasive retinal imaging and diagnosis in the clinical setting. As opposed to the conventional 800 nm Ti:Sapphire laser, fiber lasers exciting at 1.07 µm offer potential advantages over the latter. Some of said advantages have been evaluated or determined by this initial study. In particular, we have shown that contrast can be achieved in unstained thin-sliced mouse retinas and we have also provided initial spectral and temporal characterization of retinal native autofluorescence. Additionally, depth-resolved imaging of a monkey retina was done to show feasibility of our system to image in a near-*in vivo* orientation using retinas that have similar characteristics to those in humans.

The multimodal images of mouse retina in Fig. 2 show clear delineation of the different retinal layers and their different spectral signatures. The emission spectra from each of the layers are given in Fig. 3(a) and 3(b), where we are able to distinguish three main emissions. First, and best defined is the emission near 535 nm corresponding to SHG. The strongest SHG emission comes from the sclera which the protective layer of the eye and is primarily composed of collagen and elastin, both strong SHG emitters [3,52,53]. Not shown in Fig. 3(a) and 3(b) but also observed was emission at 353 nm corresponding to THG, primarily from the choroid, however, smaller amounts can be detected in the sclera and RPE. THG emission is possible from interfaces where the index of refraction changes, such as in lipid and tissue

Biomedical Optics EXPRESS

interfaces, cellular membrane boundaries, as well as highly absorptive pigments like those in the RPE [20,53–55]. THG microscopy of thin retina sections, imaged in the forward-direction configuration with a Yb-fiber laser, centered at 1044 nm, found bright signals from the ONL, INL as well as the GCL [21]. They did not image the choroid where we found the brightest THG signal in the epi direction.

In terms of 2PEF, we observe two unresolved broadband emissions one centered at ~575 nm and the other at ~629 nm. We attribute the first to lipofuscin and the latter to A2E. The emission spectra of lipofuscin and its many fluorophores are highly dependent on the excitation wavelength and tissue layer location within the retina [56,57], but generally, this emission peaks at wavelengths > 550 nm. Unfortunately, little is known regarding the isolation and characterization of all the fluorophores of lipofuscin. A2E— fluorophore of lipofuscin, is one of the few that has been characterized and is known to be a degradation product of the visual cycle [23,25,27,28,30,33,48,58–60]. Specifically, A2E is derived from phagocytosis of photoreceptor disks in the RPE that comprise the outer segments of photoreceptor cells within the ORL. Due to the nature of their functions, both the choroid and RPE have a more diverse metabolic environment [23,24,28,31,32]. Therefore, detection of a greater concentration of A2E in these regions agrees with previous studies and is expected.

In relation to the detection of FAD and NADH, the relative absence of fluorescence from FAD and NADH in our images was highly unanticipated. However, after obtaining the emission spectra and fluorescent lifetimes of pure FAD (300 μM) and NADH (350 μM) solutions with the TCSPC following direct excitation from our laser (5-minute acquisition time), the signal yield was significantly lower than any other fluorescent emissions seen in the retina. We found the expected fluorescence from NADH and FAD was present only as a result from three-photon excitation. The intrinsic low fluorescence yield of these chromophores, together with the required three-photon excitation explains their absence in our retinal images. We thus conclude FAD and NADH have negligible contributions to the emission spectra of unstained retinas with a 1.07 μm laser. The ability to isolate emission from lipofuscin and A2E from that of FAD and NADH may in fact be a significant advantage over other imaging techniques, as it is known that the levels of lipofuscin and A2E have been used to diagnose retinal disease [14,15,26].

The lifetimes plotted in Fig. 4(a)-4(c) more readily allow for comparison from one retinal layer to the next. From the NFL thru the ORL a relatively long lifetime can be seen. In contrast, a shorter lifetime is seen in the RPE and choroid. Table 1 shows fit values for these two different curves. However, these fits do not yield lifetime values that are readily comparable to literature values of known chromophores. However, from the spectral data, we find nearly identical emission spectrum can be seen from the OPL through the NFL, with a peak emission around 560 nm (approximated from the plotted spectra). In addition, a peak around 640 nm becomes prominent from the ONL to the choroid. Clearly, we are dealing primarily with two compounds, lipofuscin and A2E.

Biomedical Optics EXPRESS

**Table 2. Fitting with fixed parameters for lifetime decays shown in Fig. 4(a) and 4(b). The parenthetical values are the one standard deviation errors and have units of ns. $R^2$ is the coefficient of determination ($R^2$ error) and is a dimensionless quantity.**

| Lifetime Decays with Fixed Parameters | | | | | | | | | | | | | |
|---|---|---|---|---|---|---|---|---|---|---|---|---|---|
| | 556-594 nm | | | | | | 610-648 nm | | | | | |
| ORL through NFL | Bi Fit (ns) | | | | | | Bi Fit (ns) | | | | | |
| | $a_1$ | $t_1$(ns) | $a_2$ | $t_2$(ns) | $R^2$ | | $a_1$ | $t_1$(ns) | $a_2$ | $t_2$(ns) | $R^2$ | |
| | 0.401 (0.008) | 0.390 (Fix) | 0.599 (0.008) | 2.24 (Fix) | 0.98 | | 0.446 (0.005) | 0.390 (Fix) | 0.554 (0.005) | 2.24 (Fix) | 0.99 | |
| Choroid and RPE | Bi Fit (ns) | | | | | | Bi Fit (ns) | | | | | |
| | $a_1$ | $t_1$(ns) | $a_2$ | $t_2$(ns) | $R^2$ | | $a_1$ | $t_1$(ns) | $a_2$ | $t_2$(ns) | $R^2$ | |
| | 0.657 (0.005) | 0.170 (Fix) | 0.343 (0.005) | 1.3 (Fix) | 0.99 | | 0.761 (0.004) | 0.170 (Fix) | 0.239 (0.004) | 1.3 (Fix) | 0.99 | |
| | Tri Fit (ns) | | | | | | Tri Fit (ns) | | | | | |
| | $a_1$ | $t_1$(ns) | $a_2$ | $t_2$(ns) | $a_3$ | $t_3$(ns) | $R^2$ | $a_1$ | $t_1$(ns) | $a_2$ | $t_2$(ns) | $a_3$ | $t_3$(ns) | $R^2$ |
| | 0.512 (0.023) | 0.170 (Fix) | 0.207 (0.020) | 0.390 (Fix) | 0.212 (0.004) | 2.24 (Fix) | 1 | 0.810 (0.020) | 0.170 (Fix) | 0.079 (0.018) | 0.390 (Fix) | 0.152 (0.004) | 2.24 (Fix) | 1 |

We repeated the fits presented in Table 1, this time holding the lifetimes constant to values found in the literature for lipofuscin and A2E [29]. In Table 2, for the ORL to NFL, a bi-exponential fit works well when $t_1$ = 0.39 ns and $t_2$ = 2.24 ns are fixed, which corresponds to the bi-exponential values for lipofuscin in the literature [29]. In the RPE and choroid curve, a tri-exponential fit works well when $t_1$ = 0.17 ns, $t_2$ = 0.39 ns and $t_3$ = 2.24 ns are fixed, where $t_1$ corresponds to the literature value for the lifetime of A2E, and $t_2$ and $t_3$ are the lifetimes associated with lipofuscin [29]. Additionally, in the RPE and choroid curve, a bi-exponential fit is performed where $t_1$ = 0.17 ns and $t_2$ = 1.3 ns. Here, $t_1$ is again the lifetime of A2E and $t_2$ is approximately the value of the mono-exponential fit for the ORL to NFL curve. Note that we find a greater contribution from A2E in the RPE and choroid. We also attribute the signals detected in the NFL to the ORL to either lipofuscin or one of its degradation products. The presence of degradation products could explain why an emission peak can be seen at 629 nm emission in the ONL, ORL and IRL, yet these layers do not show a short lifetime found for those signals in the RPE and choroid. To confirm that A2E can be readily excited with a 1.07 μm laser, we measured the spectrum and lifetime of a solution of A2E. The emission was very strong and the spectral shape and lifetime agreed with the literature and the emission from the retina (See Appendix 2). Lipofuscin is very hard to isolate; therefore, we were unable to measure it in solution. In addition to lipofuscin and A2E, other known fluorescent compounds in the retina, including rhodopsin, all-*trans*-retinal, and melanin, could contribute to the signals observed. Gathering our spectral and lifetime findings we are able to conclude that multimodal signals correspond to THG, SHG and TPEF from lipofuscin and A2E. We find that the deeper retinal layers, where the receptors are concentrated, contain greater amounts of A2E.

Our results include the first depth resolved multimodal images of monkey retina obtained in the ep-direction. The images from the stack show excellent sub-cellular resolution, making it easy to distinguish among the different cell types in each layer. The robust signals detected bode well for the use of multimodal microscopy with a femtosecond Yb-fiber laser source for future retinal diagnostics.

The composite images in Fig. 2, their corresponding emission spectra (Fig. 3(a) and 3(b)), as well as the lifetime measurements (Fig. 4(a)-4(c)) come from one retina. However, similar measurements were performed on 9 total retinas (5 fixed, 4 unfixed). All measurements were performed with identical image acquisition times to ensure consistency amongst the samples. The results from those measurements are consistent with the findings of this work. We acknowledge that these are very preliminary studies and more studies will need to be completed prior to claiming this system as ready for clinical use. Furthermore, future studies should address differences in the retina from different animals (both sexes) for both healthy

Biomedical Optics EXPRESS

and for a few of the most common diseases. However, these initial findings presented here establish the feasibility for the overall goal.

## 5. Conclusions

In summary, we presented the first epi-direction multimodal imaging of unstained isolated mouse and Cynomolgus monkey retinas with an ultrafast fiber laser centered at 1.07 µm. Measurements of the fluorescence spectra and lifetime from a thin cross-section of a mouse retina showed that emission from the ORL to the NFL have similar spectra, including a relatively long lifetime. The RPE and choroid have similar spectra, including a relatively short lifetime. We attribute a majority of the short lifetime signal to A2E, and a majority of the long lifetime signal to lipofuscin or other lipofuscin degradation products. Interestingly, we show that FAD and NADH do not significantly contribute to the fluorescence emission from a 1.07 µm laser. This is different from most multiphoton microscopy studies where FAD and NADH are usually the strongest autofluorescent signals. In addition, depth resolved imaging of an unstained Cynomolgus monkey retina is also presented using the same laser and experimental setup. The depth resolved images from the Cynomolgus monkey show that it is feasible to use our collection system to image the retina of live-animal subjects, and in the future of humans.

## Appendix 1

### *Extra Information on the fits*

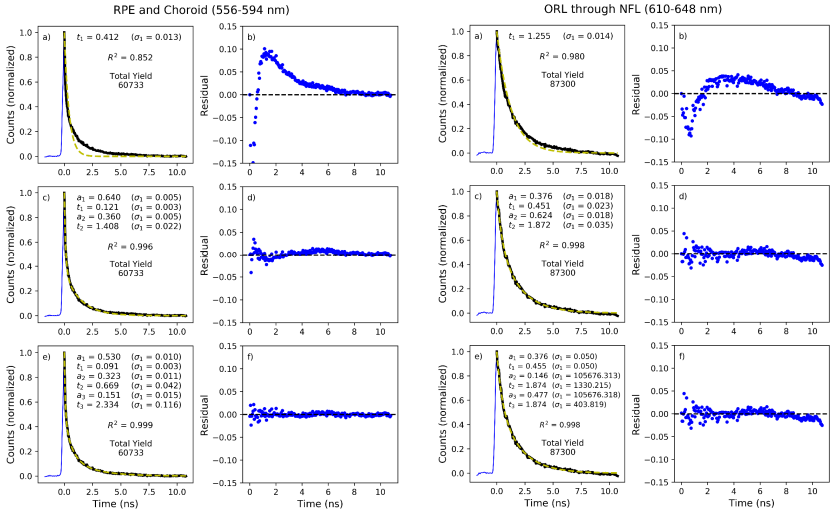


Fig. 6 (Left). Lifetime decay fits and the corresponding residual plots for the RPE and choroid for the wavelength range of 556-594 nm. This figure shows the RPE and choroid fit poorly to a mono-exponential function. (Right). Lifetime decay fits and the corresponding residual plots for the ORL through NFL for the wavelength range of 610-648 nm. This figure demonstrates that the ORL-NFL layers fit poorly to a tri-exponential function

Figure 6 left and right show selected representative cases of how the criteria for excluding a certain fit type were. For the ORL through the NFL the tri-exponential fits were discarded in Table 1 as the values for $t_2$ and $t_3$ were identical (Fig. 7). In Table 2, where the wavelengths were held fixed, the value for $a_1$ in the fits became negative. For the choroid and RPE, the mono-exponential fits were discarded as the $R^2$ value was always below 0.91 (Fig. 6 right), which is well below the lowest accepted $R^2$ value in either of the tables ($R^2 \geq 0.98$) in this work.

Biomedical Optics EXPRESS

## Appendix 2

### *A2E solution measurements*

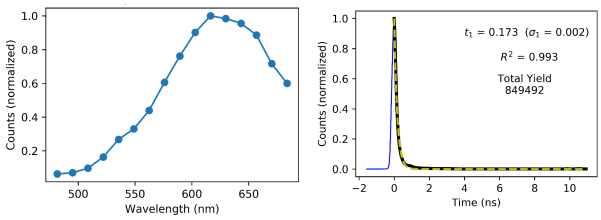


Fig. 7. The spectra (Left) and lifetime (Right) from a 1 mM solution of A2E. The spectra peaks near 625 nm, which is the same peak seen in the choroid, RPE, and receptor layers. The lifetime of ~173 ps agrees with the literature values [29].

The emission spectrum of A2E is highly dependent on the excitation wavelength [34]. Therefore, we measured an isolated 1 mM solution to more accurately compare with the retina data. Our measurements show that the A2E solution has a peak wavelength ~625 nm, which is the same peak that can be seen in the choroid, RPE, and receptor layers. It is worth noting that the dichroic that was used to separate the fundamental from the fluorescence in the retina data starts to decrease in transmission at wavelengths greater than 650 nm. By the time the A2E solution was measured this optic had been replaced with one that has an edge at 750 nm. The lifetime was measured from the range ~600-670 nm. The value of ~173 ps agrees well with the literature value [29].

## Acknowledgements

We thank Dr. Zhiqian Dong (Polgenix Inc.) for his technical help on animal experiments and Krzysztof Palczewski, Chief Scientific Officer (Polgenix Inc.). We also thank Julio Cesar Corral-Serrano and Dr. Rob Collin (Radboud University Medical Center, Nijmegen, The Netherlands) for kindly sharing their unfixed mouse retinal section protocol. Partial funding of this work came from the National Science Foundation under grant CHE1464807 for the development of novel spectroscopic methods (M.D.). In addition, this work was supported by funding from the National Institutes of Health EY025451 (K.P.).

## Disclosures

MD Biophotonic Solutions Inc. and IPG Photonics (C, P), GP Polgenix Inc. (I, E), KP Polgenix Inc. (I. S). All other authors declare that there are no conflicts of interest related to this article.